



Synthesis of Magnetically Recoverable Ru/Fe₃O₄ Nanocomposite for Efficient Photocatalytic Degradation of Methylene Blue

Avvaru Praveen Kumar¹ · Faheem Ahmed² · Shalendra Kumar^{2,3} · G. Anuradha¹ · Kalla Harish⁴ · Begari Prem Kumar⁵ · Yong-Ill Lee⁶

Received: 25 June 2021 / Accepted: 29 July 2021 / Published online: 12 August 2021

© The Author(s), under exclusive licence to Springer Science+Business Media, LLC, part of Springer Nature 2021

Abstract

Photocatalytic degradation of pollutants is considered to be an effective green method to remove organic dyes from contaminated water. This research work presents the synthesis of a magnetically recoverable ruthenium-magnetite (Ru/Fe₃O₄) nanocomposite for the photocatalytic degradation of methylene blue (MB) in an aqueous solution under UV and sunlight radiation. The magnetic Ru/Fe₃O₄ nanocomposite is synthesized in a single step using the chemical co-precipitation method. The synthesized nanocomposite sample is characterized by various techniques, including, XRD, FT-IR, SEM, TEM, TEM-EDX, XPS and VSM whereas the photocatalytic degradation of MB is analyzed by the UV-Vis spectrophotometer. The formation of ruthenium nanoparticles in magnetic Fe₃O₄ has been confirmed by TEM, TEM-EDX and XPS studies. The catalytic activity of the synthesized Ru/Fe₃O₄ nanocomposite is evaluated by photodegradation of the MB dye aqueous solution under UV and sunlight radiation. The influences of various operation parameters on photocatalytic degradation such as pH, dye initial concentration and catalyst dosage are examined. The results revealed a complete photocatalytic degradation of MB in the aqueous solution occurred by exposure to both UV and sunlight radiation. Furthermore, the photocatalytic degradation of MB under UV light is faster than sunlight. The photocatalytic degradation reaction of MB is found to be consistent with the pseudo-first-order kinetics. The strong ferromagnetic nature of Fe₃O₄ enables the nanocomposite to be separated from the solution for recycling and has a photocatalytic efficiency of greater than 90% for up to five cycles. The synthesized Ru/Fe₃O₄ photocatalyst efficiently degrades MB dye, so it can be used as a potential catalyst for the removal of MB in aqueous solutions.

✉ Avvaru Praveen Kumar
drkumar.kr@gmail.com

¹ Department of Applied Chemistry, School of Applied Natural Science, Adama Science and Technology University, Po Box 1888, Adama, Ethiopia

² Department of Physics, College of Science, King Faisal University, P.O. Box 400, Al-Ahsa 31982, Saudi Arabia

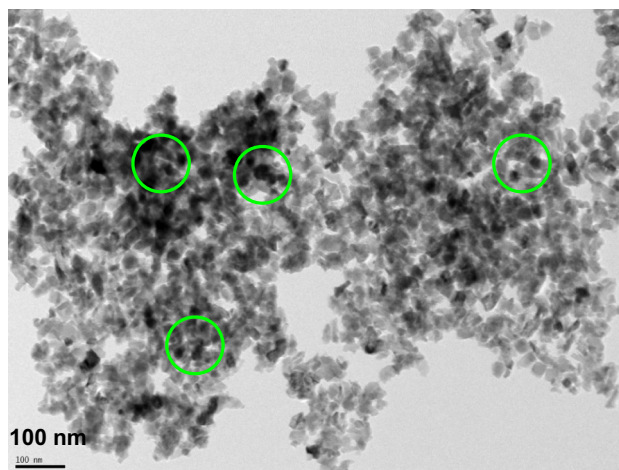
³ Department of Physics, University of Petroleum and Energy Studies, Dehradun 248007, India

⁴ Department of Electronics and Communication Engineering, Adama Science and Technology University, Po Box 1888, Adama, Ethiopia

⁵ Research and Development, Tata Steel Limited, Jamshedpur 831001, India

⁶ Department of Chemistry, Changwon National University, Changwon 51140, Republic of Korea

Graphic Abstract



Keywords Ru · Fe₃O₄ nanocomposite · Characterization · Photocatalytic degradation · Methylene blue · UV and sunlight irradiation

Introduction

Water pollution is one the major environmental problem throughout the world. Ground water and surface waters are becoming polluted and this is due to population growth in recent years. Water pollution is mainly caused through contamination of water which arising from dyes, textile industries, fertilizers, industrial chemicals, food and domestic wastes [1]. Water contaminated with organic dyes can lead to high toxicity, which can have harmful and carcinogenic effects on living beings, even in small quantities [2]. Furthermore, metabolites derived from organic dye compounds are more harmful than parent dye molecules [3]. Some organic pollutants have been reported to be biologically purified in natural water sources [4], while most dye pollutants are not degradable and are not biologically purified [5]. Therefore, these pollutants remain in the environment for a long time, causing toxic effects not only on humans but also on ecosystems. Methylene blue (MB) is a thiazine dye that has a wide range of industrial applications, including as a dye to tone up silk colors, cotton, wool, leather, paper and jute, and as a food coloring additive [6, 7]. MB dye is also used in the aquaculture industry as a chemotherapeutic and anti-malarial agent [8]. Due to its hydrophilic nature and complex aromatic structures it is not degraded by conventional water purification process and is also stable to temperature, light, water etc. The accumulation of MB dye in the environment is

highly toxic and can cause serious environment pollution. Hence, hazardous organic dyes should be eliminated from industrial effluents.

In recent decades, many methods have been reported to remove the organic dye contaminants from water and aqueous effluents. Some techniques have been used effectively such as coagulation and flocculation [9], membrane processes [10], biological treatment [11], adsorption process [12], ion exchange [13], photosensitized chemical oxidation [14], photocatalytic degradation [15] and electrochemical treatment [16]. Nevertheless, some drawbacks of these methods are the production of secondary waste products, which cannot be retreated or dumped [17, 18], as well as high costs, time consumption, and partial effectiveness [19]. Among these diverse methods, photocatalysis has attracted considerable attention to the degradation of dyes in industrial effluents [20, 21]. Photocatalysis is an advanced oxidation process that oxidizes toxic pollutant dyes into small inorganic molecules (CO₂ and H₂O) in the presence of light and purifies the wastewater. Moreover, this reaction is thorough and does not cause secondary pollution [22]. So, photocatalysis is an interesting and alternate method which can be used for the degradation of dyes in wastewater and also for cleaning the environment [20, 21].

In recent years, nanoparticles (NPs) have been used to eliminate toxic dyes from wastewater and have shown significant advancement due to their high adsorption properties, large surface area, faster rates of equilibrium

and low resistance to diffusion [20, 21, 23]. Among a wide variety of nanomaterials for environmental applications, the magnetite (Fe₃O₄) based NPs have received much attention due to magnetic properties. Magnetic nanostructures can be altered by applying a magnetic field [24], which can lead to numerous applications such as magnetic resonance imaging, lithium storage capacity, drug delivery systems, cancer treatment, photocatalysis, biological separation, wastewater treatment, hyperthermia, etc. [25–27]. At the same time, Ruthenium (Ru) NPs have been shown to be potential catalysts for different catalysis-based applications [28–31]. Ru NPs can increase the efficiency of photo-excited electron–hole pair separation due to their quantized nature and thereby enhance the photocatalytic activity of nanocomposites. In the literature, some Fe₃O₄ and/or Ru based nanocomposites have been reported in recent years for photocatalytic degradation of dyes [32–36]. Długosz et al. [32] synthesized Fe₃O₄/ZnO NPs for photocatalytic degradation of anionic and cationic dyes, and it has been observed that dyes undergo high photodegradation as their molar mass increases. Shanker's research group [33] developed recyclable g-C₃N₄-Fe₃O₄ nanocomposites to show improved photocatalytic activity and Sahoo et al. [34] reported a separable g-C₃N₄/Fe₃O₄/porous Ru nanocatalyst for photodegradation of water-soluble azo dyes and aromatic amines. The photocatalytic degradation was performed under visible light in both studies [33, 34]. Ru–TiO₂ semiconducting NPs were synthesized by the Kulkarni research team [35] for the photocatalytic degradation of bromothymol blue and they studied the effect of BTB amount, Ru–TiO₂ dosage, UV light intensity and pH on the degradation rate. Recently, a sonochemical activation-assisted biosynthesis of Au/Fe₃O₄ NPs has been reported for sonocatalytic degradation of methyl orange [36]. There are no reports on Ru/Fe₃O₄ NPs for photocatalytic degradation of dye pollutants in the literature survey.

The current work describes a chemical co-precipitation technique for the synthesis Ru/Fe₃O₄ nanocomposite in a single step. The chemical co-precipitation method has many advantages such as variety of precursor selections to choose as starting materials, easy handling, a high degree of homogenization together with a small particle size, ambient processing temperatures, cost effective and easy to set-up and large scale production compared to other synthesis methods like sol–gel, hydrothermal, auto combustions etc. [37, 38]. The synthesized Ru/Fe₃O₄ nanocomposites were characterized by various instruments to study morphology, chemical, structural and magnetic properties. Then, photocatalytic activity of as-synthesized Ru/Fe₃O₄ nanocomposites was performed on the degradation MB dye using various operational parameters, including irradiation time, effect of pH of the MB solution,

initial MB concentration, amount of photocatalyst, and kinetics of photodegradation.

Experimental

Preparation of Ru@Fe₃O₄ Nanocatalysts

A chemical co-precipitation method was employed to synthesize Ru@Fe₃O₄ nanocomposites in a single step, briefly described as: The prepared solutions, 0.05 M of ruthenium trichloride hydrate (RuCl₃·H₂O, Aldrich-40.1% Ru) and 0.1 M of ferric nitrate nonahydrate (Fe(NO₃)₃·9H₂O, Aldrich) were mixed in a beaker under uniform stirring at room temperature. Then, a 0.1 M Na₂CO₃ solution was added drop wise to the reaction solution, and the pH of the resultant solution was 9. The reaction mixture was stirred magnetically for 24 h and the resulting precipitate was allowed to settle. A magnet field was applied using a magnet to isolate the precipitate for the washing step. The isolated precipitate was filtered, washed several times using deionized water and then dried under vacuum at 50 °C overnight. Finally, the dried precipitate was calcined at 300 °C under nitrogen (N₂) atmosphere for 3 h to produce a black powder material of Ru@Fe₃O₄ nanocomposite particles.

Characterization of the Nanocatalysts Sample

The X-ray diffraction (XRD) technique was performed by Philips X'pert MPD 3040 with Cu K α radiation over a 2θ range from 20° to 80° at 2.5° per minute. A Nicolet FT-IR 400 spectrometer (Nicolet iS10, SCINCO, USA) was used to obtain the Fourier Transform Infrared (FTIR) spectra and the sample was prepared by KBr pellet method. The surface morphology of the nanocomposite was recorded by a field emission scanning electron microscope (FE-SEM-MIRA II, LMH) operating at an accelerated voltage of 20 kV. A transmission electron microscope (TEM, JEM-2100F, JEOL, Japan) was executed to see the morphology of nanocomposites and energy dispersive X-ray (EDX) analysis was carried out to ascertain the elemental analysis of the sample. The X-ray photoelectron spectroscopy (XPS) was carried out by a MultiLab2000 (Thermo VG Scientific, USA). The pore size distributions, pore volume and surface area were determined by N₂ adsorption–desorption isotherms using Autosorb-1 equipment (Quantachrome, USA). The pore size distribution and surface area were measured by Brunauer–Emmett–Teller (BET) method. The UV–Vis spectra were acquired by a Lambda 950 spectrometer (Perkin Elmer). A vibrating sample magnetometer (VSM, Lakeshore 7304) was used to

estimate the magnetic properties of Ru@Fe₃O₄ magnetic nanocomposite samples at room temperature.

Photocatalytic Degradation

To assess the photocatalytic degradation performance of as-synthesized Ru@Fe₃O₄ nanocomposites, the photodegradation experiments were conducted on MB dye solution at room temperature in the absence of light and in the presence of sunlight and UV-light (Philips 8 W, E_{max} = 254 nm). The typical photocatalytic degradation was carried out as follows: a required amount of magnetic nanocomposite photocatalyst was added to a 100 mL of MB dye aqueous solution (30 mg/L). Subsequently, the resulting suspension was stirred magnetically in the dark for 30 min to establish the adsorption–desorption equilibrium between photocatalyst and MB dye. The samples were then subjected to sunlight or UV light lamp in separate experiments. The photocatalytic degradation of the MB dye reaction was monitored at various time intervals by recording the absorbance at λ_{max} of the MB dye at a specific wavelength using UV–Vis spectrophotometer. All the measurements were conducted in duplicate and performed a third time when necessary. A similar experimental procedure was used for control experiments. The photocatalytic degradation rate can be calculated as follows:

$$\text{Degradation rate (\%)} = [(A_0 - A/A_0)] \times 100$$

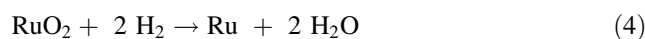
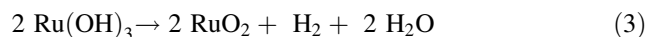
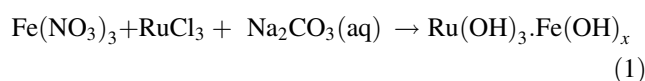
$$\text{Degradation rate (\%)} = [(C_0 - C/C_0)] \times 100$$

where A₀ represents the initial absorbance of the MB solution, A shows the absorbance of the MB solution after light irradiation at time t, C₀ is the initial concentration of the MB solution and C is the concentration of the MB solution after light irradiation at time t.

Results and Discussions

Characterization of Ru/Fe₃O₄ Magnetic Nanocomposite

The Ru/Fe₃O₄ magnetic nanocomposite was synthesized in a single step using a chemical co-precipitation technique. The obtained sample of Ru(OH)₃.Fe(OH)_x was reduced in a nitrogen atmosphere at 300 °C to get pure Ru/Fe₃O₄ nanocomposites. The chemical reactions that occur during the formation of Ru/Fe₃O₄ nanocomposites are represented in the following equations:



The results of the synthesized nanocomposite are discussed as follows.

The crystalline nature and crystal phase of as-synthesized Ru/Fe₃O₄ nanocomposite were examined by powder XRD experiments and results are shown in Fig. 1a. The typical XRD pattern of the nanocomposite displays the various well defined diffraction reflections detected at (2θ): 30.1, 35.4, 43.2, 53.5, 57.1, 62.8 and 74.3° correspond to crystalline planes of (220), (311), (222), (400), (422), (511), (440) and (533), respectively [39]. The peaks appeared sharp and strong, indicating the formation of well crystallized Fe₃O₄ with a cubic lattice structure. Apart from Fe₃O₄, no peaks representing to Ru were detected in the XRD pattern of Ru/Fe₃O₄ nanocomposite. This indicates that the metallic Ru nanoparticles were uniformly dispersed to obtain Ru/Fe₃O₄ photocatalysts after calcinating the nanocomposite sample in the nitrogen environment. Furthermore, no other peaks of contaminants were found in the XRD pattern, suggesting the formation of highly pure Ru/Fe₃O₄ photocatalysts.

The FTIR spectrum of magnetic Ru/Fe₃O₄ nanocomposite was presented in Fig. 1b. In the FTIR spectrum, a characteristic absorption band observed at 566 cm⁻¹ is assigned to the vibration of Fe–O of Fe₃O₄ [40]. Apart from this, two other peaks were detected at 1624 cm⁻¹ and 3410 cm⁻¹ related to the stretching vibration of hydroxyl groups (-OH) [41, 42] absorbed on the surface of nanocomposite. The existence of these hydroxyl absorption peaks is due to absorption of moisture during testing of the nanocomposite sample.

The morphology of the synthesized Ru/Fe₃O₄ nanocomposites was examined by FE-SEM. The SEM images at two different magnifications are displayed in Fig. 2a & b. SEM pictures clearly show nanocomposite particles that are uniformly distributed with small size and it has been observed that these particles are spherical in shape. The TEM image of the magnetic Ru/Fe₃O₄ nanocomposite sample was shown in Fig. 2c which reveals that the Ru NPs are highly dispersed over Fe₃O₄. Also, the synthesized Ru/Fe₃O₄ nanocomposite has an aggregated form of structure and this aggregation may be due to magnetic dipole–dipole interactions between the nanosized particles [43]. The analysis for distribution of particle size was performed to measure the bulk features of the aggregated NPs. As per the analysis the average diameter of the

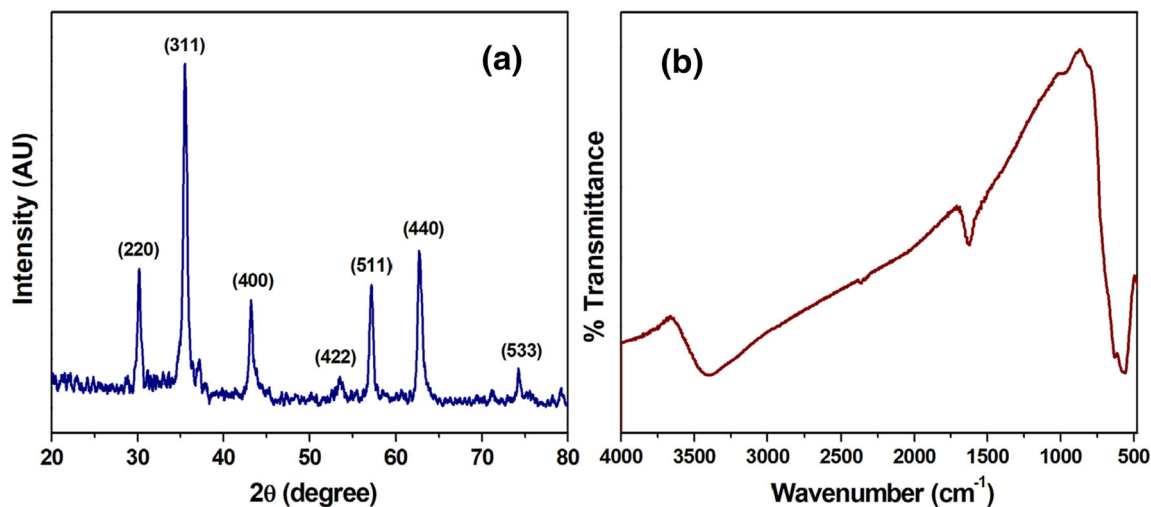


Fig. 1 **a** XRD pattern and **b** FT-IR spectrum of Ru/Fe₃O₄ nanocomposite

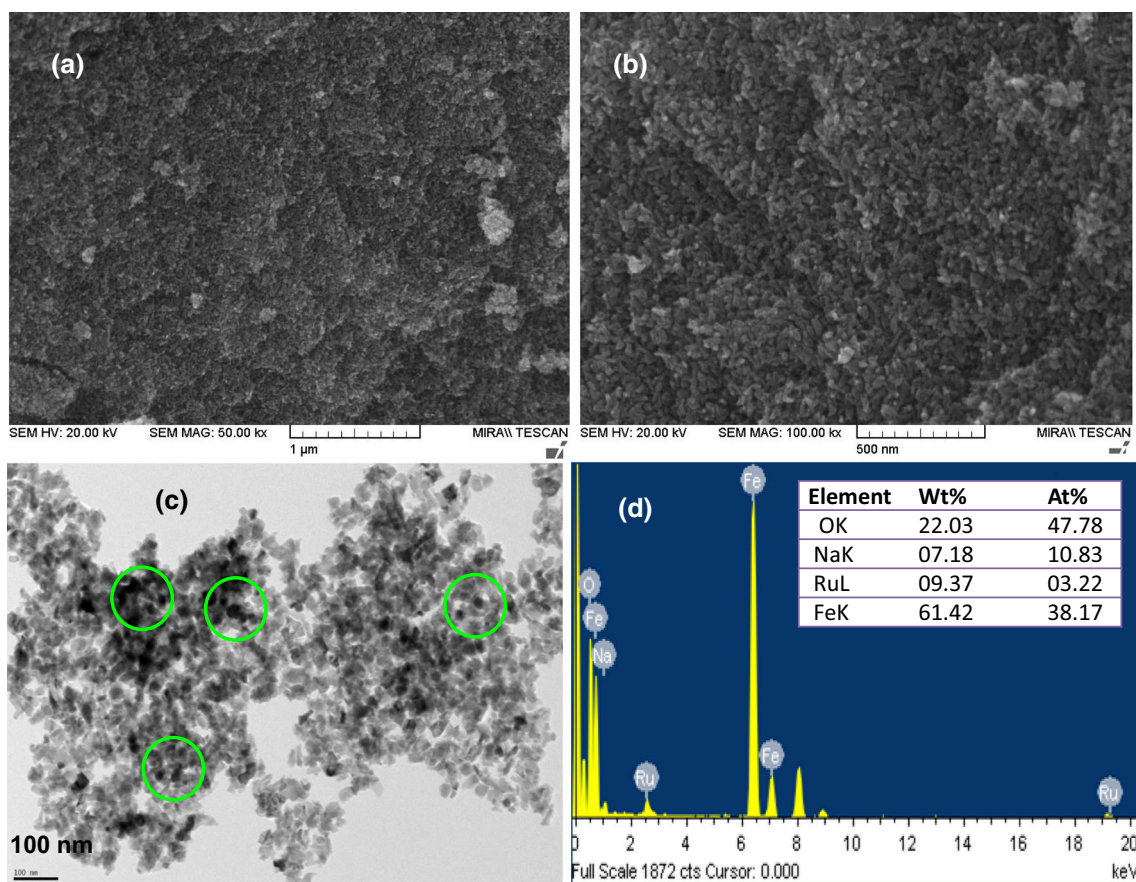


Fig. 2 **a**, **b** SEM images, **c** TEM image (inside the circles show the formed Ru NPs) and **d** TEM-EDX spectrum of Ru/Fe₃O₄ nanocomposite

particle was estimated to be 31.5 nm and the Ru NPs size was not in uniform (between 5 to 8 nm) but the Ru NPs were well dispersed. This further indicates that the Ru species fused on magnetite during calcination. Figure 2d displays the TEM-EDX spectrum of Ru/Fe₃O₄ nanocomposite, which confirms the dispersed Ru metal content of

9.04 wt %, 61.42 wt % of Fe and 22.03 wt % of O in the magnetic Ru sample.

XPS is a powerful technique that can be used to examine the chemical composition of nanomaterials. Figure 3a & b provides high resolution (HR) XPS spectra of Fe 2p region and Ru 3d region. As seen in HR-XPS spectrum (Fig. 3a),

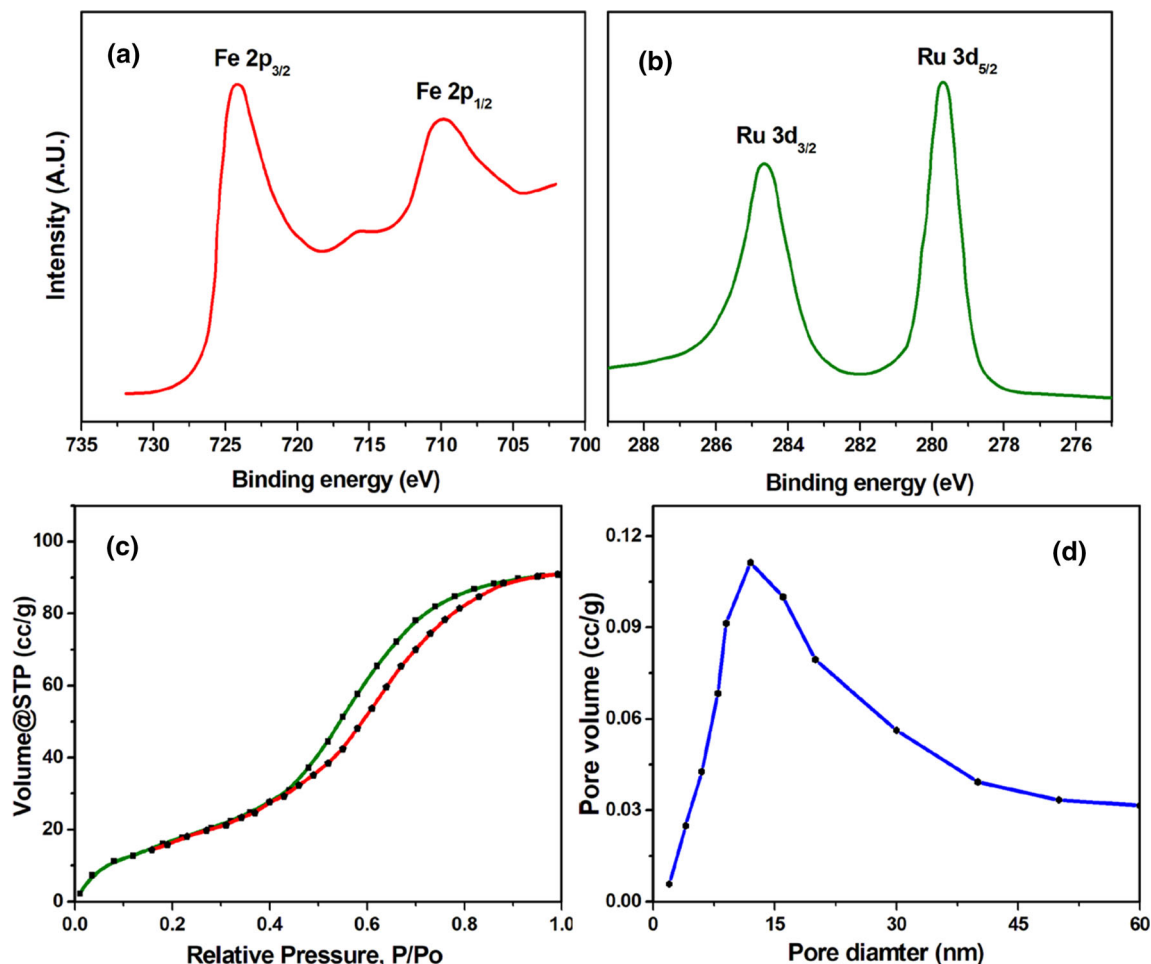


Fig. 3 HR-XPS spectra: **a** Fe 2p region and **b** Ru 3d region of nanocomposite, **c** N_2 adsorption-desorption isotherms and **d** Pore size distribution of Ru/Fe_3O_4 nanocomposite

the Fe 2p region shows two peaks at binding energies 709.9 eV and 724.2 eV which belong to Fe $2p_{3/2}$ and Fe $2p_{1/2}$, respectively. The energy difference between these Fe $2p_{3/2}$ and $2p_{1/2}$ peaks (spin-orbit splitting) is close to the standard value, which ensures the formation of Fe_3O_4 NPs [44, 45]. The formation of Ru species and its oxidation state in the Ru/Fe_3O_4 nanocomposite are confirmed by XPS. The HR-XPS spectrum (Fig. 3b) of the nanocomposite sample shows two prominent Ru peaks at binding energies of 284.1 and 297.2 eV. These two peaks can readily be attributed to Ru(0) $3d_{3/2}$ and $3d_{5/2}$, respectively, indicating the existence of metallic Ru(0) in its elementary state by comparison with the values of metallic ruthenium [46, 47].

The BET method can be used to measure the specific surface area and porous nature of the magnetic Ru/Fe_3O_4 photocatalysts by estimating the amount of nitrogen gas adsorbed on the surface of photocatalysts. Figure 3c shows the nitrogen adsorption-desorption isotherm and Fig. 3d displays the pore size distribution curve of Ru/Fe_3O_4

photocatalysts. The BET specific surface area and pore volume of the Ru/Fe_3O_4 photocatalysts were observed to be $90.5 \text{ m}^2 \text{ g}^{-1}$ and $0.16 \text{ cm}^3 \text{ g}^{-1}$, respectively. A type-IV isotherm was observed which indicates the mesoporous nature of the synthesized photocatalysts. The pore size distribution plot (Fig. 3d) shows well-developed mesopores with a diameter of 12.2 nm, which supported the porous nature of the Ru/Fe_3O_4 photocatalysts according to the BJH model. This suggests that the properties of synthesized photocatalysts could provide more active sites for the occurrence of photocatalytic reactions.

The UV-Vis DRS spectrum of the Ru/Fe_3O_4 nanocomposite was displayed in Fig. 4a. The DRS method was performed to study the optical absorption behavior and to determine the band gap energy for photocatalysts. It can be seen in Fig. 4a, wide absorption was observed in the range of 250 nm to 402 nm within 500 nm for Ru/Fe_3O_4 nanocomposite. The band gap energy of Ru/Fe_3O_4 nanocomposites was calculated by Tauc and Davis-Mott relation [48] as given below.

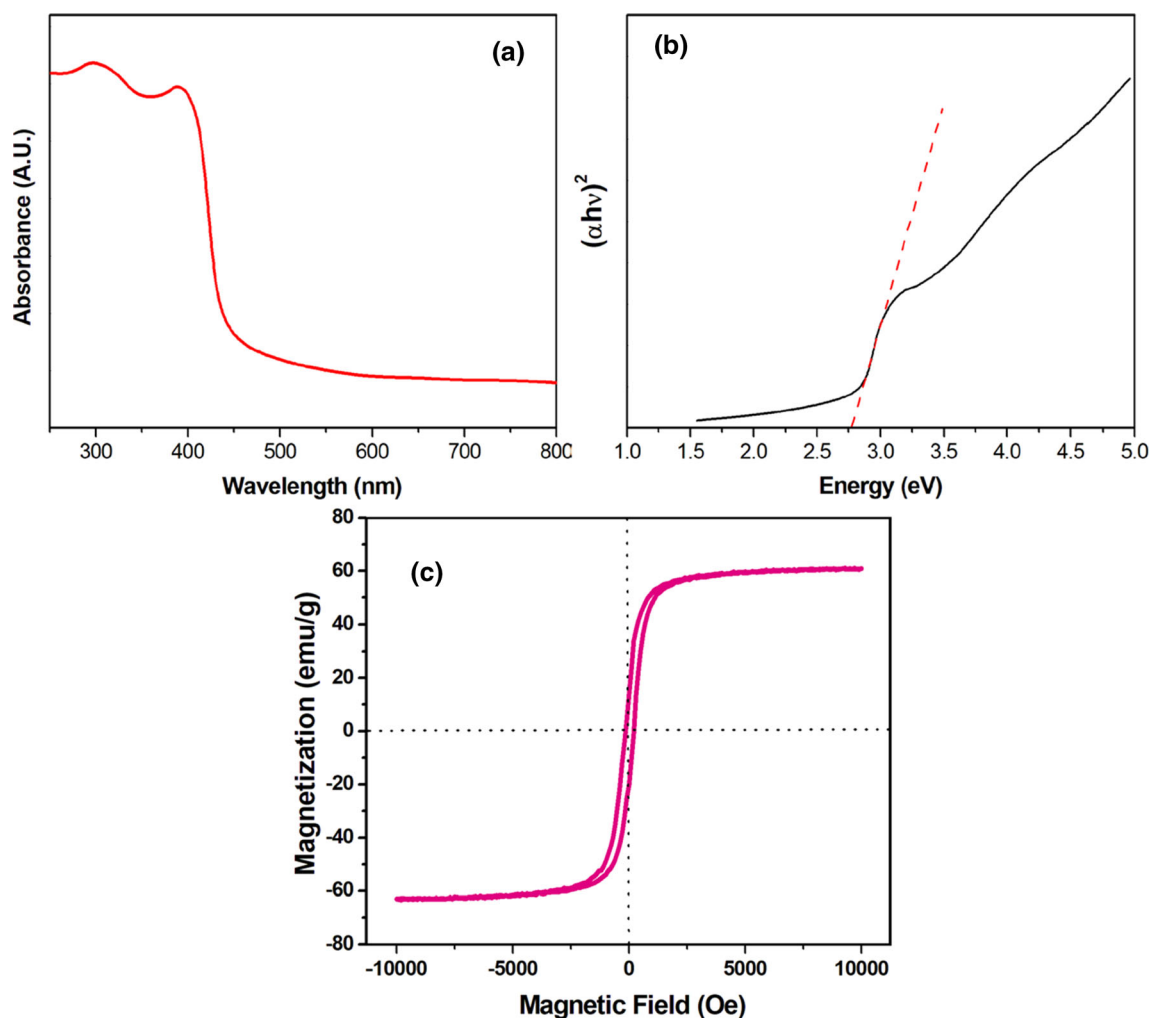


Fig. 4 **a** UV-Vis DRS, **b** Tauc plot and **c** magnetization curve of Ru/Fe₃O₄ nanocomposite

$$(\alpha h\nu)^n = K (h\nu - E_g)$$

where α is the absorption coefficient, $h\nu$ is the incident photon energy, K is the energy independent constant, E_g is the band gap energy and $n = 1/2$ corresponding to the allowed direct transitions. The E_g is calculated from plotting $(\alpha h\nu)^{1/2}$ against $h\nu$, by extrapolating the straight line portion of the curve to the zero coefficient value. The Tauc plot (Fig. 4b) suggested that the band gap energy for Ru/Fe₃O₄ nanocomposites is 2.78 eV. This could allow for better UV light-harvesting capability of Ru/Fe₃O₄ nanocomposites for photocatalytic applications.

VSM was performed to study the magnetic behavior of Ru/Fe₃O₄ photocatalysts at room temperature. The curve of magnetization versus magnetic field (hysteresis loops) of the photocatalysts was presented in Fig. 4c. The absence of hysteresis at the room-temperature magnetization was observed that reveals the superparamagnetic character of the synthesized Ru/Fe₃O₄ photocatalysts. Using an external field of 10 kOe, the saturation magnetization value of Ru/

Fe₃O₄ photocatalysts was determined to be 62.6 emu g⁻¹. These magnetic Ru nanocomposites exhibited negligible coercivity and remanence, indicating the distinctive role of superparamagnetic materials. Moreover, these superparamagnetic Ru/Fe₃O₄ nanocomposites can be easily separated from the liquid medium by applying a magnetic field using a permanent magnet. This suggests that magnetic Ru nanocomposites have an excellent magnetic responsivity and redispersibility, which is beneficial for their chemical and biological applications.

Photocatalytic Degradation of MB

The photocatalytic activity studies of the synthesized Ru/Fe₃O₄ nanocomposite are evaluated by measuring the degradation of MB in an aqueous solution under UV light and sunlight irradiation. The photocatalytic reaction solution was left for 30 min to achieve absorption-desorption equilibrium under dark conditions. The time-dependent

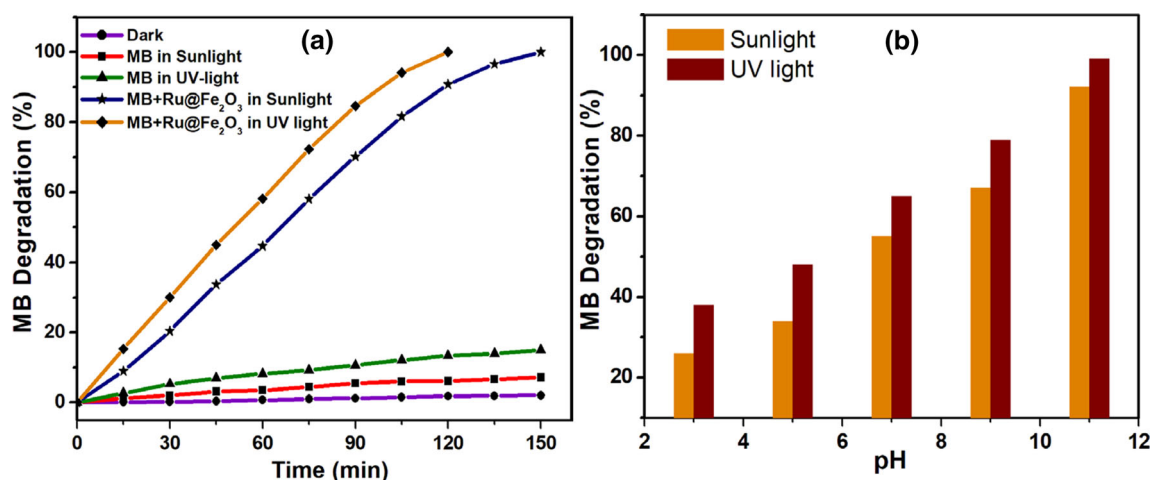


Fig. 5 a Photocatalytic degradation of MB using Ru/Fe₃O₄ catalysts and b effect of pH on the photocatalytic degradation of MB

photocatalytic degradation curves of the MB dye solution in UV and sunlight irradiation are shown in Fig. 5a, which demonstrates that the rate of degradation increases with increasing irradiation time. The complete (100%) MB dye photocatalytic degradation was observed within 120 and 150 min, respectively, during UV and sunlight exposure. Control experiments, including MB dye in the dark, in UV and sunlight without addition of Ru/Fe₃O₄ catalysts were performed to find out if any degradation had occurred. As seen in Fig. 5a, almost no degradation occurs under dark conditions, but degradations of 8% and 5% were observed under UV and sunlight irradiation, respectively. These experiments suggest that very poor photocatalytic degradation is possible only in the absence of Ru/Fe₃O₄ photocatalysts in both UV and Sunlight. This clearly evidences that Ru/Fe₃O₄ photocatalysts are required for photodegradation of MB pollutant. Also, a solution containing Ru/Fe₃O₄ photocatalysts along with MB dye was kept in the dark, and it was observed that the degradation solution was stable in the dark and no noticeable adsorption took place. This indicates that the degradation process of MB occurs only under UV/sunlight exposure with Ru/Fe₃O₄ photocatalysts. From the results of photocatalytic degradation with respect to time, it can be concluded that both UV and sunlight degradations achieved superior photocatalytic degradation efficiency towards MB dye by the prepared Ru/Fe₃O₄ composites. And greater photocatalytic degradation was observed in UV light compared to sunlight. Further, the effects of other operational parameters, such as the pH of the MB dye solution, the MB dye concentration in the solution, the kinetics of the photocatalytic reaction and the amount of Ru/Fe₃O₄ photocatalyst in the solution were investigated on the MB dye degradation efficiency. Besides, the mechanism of photocatalytic degradation and reuse of the Ru/Fe₃O₄ photocatalysts are researched and discussed.

The pH of the degradation solution is an important parameter on the efficiency of the photocatalytic reaction. The effect of pH on the degradation efficiency of MB in UV and sunlight was investigated within the pH range of 3 to 11. The pH of the photodegradation solutions was adjusted using dilute aqueous HCl and NaOH solutions. As seen in Fig. 5b, photocatalytic degradation increases with pH, which clearly represents higher pHs (alkaline medium) giving better results than the neutral pH and the acid medium. The highest degradation percentage of MB at alkaline pH values can be explained as follows: in an acidic medium (pH < 7) photocatalysts get H⁺ ions and become a positively charged surface and methylene blue is a cationic dye, so, both acquire a positive charge, resulting in less adsorption. On the other hand, as the pH of the degradation solution increases, the concentration of hydroxyl ions increases, resulting in enhanced radical hydroxyl formation. These hydroxyl radicals are very reactive and act as oxidizing agents in the advanced oxidation processes, and are more favorable for greater photocatalytic activity at higher pHs [49]. In addition, the electrostatic attraction between the cationic MB species and the negatively charged Ru/Fe₃O₄ photocatalysts enhances the adsorption rate of the MB species on the surface of Ru/Fe₃O₄ photocatalysts. This leads to a positive effect on the photocatalytic degradation of MB dye. Therefore, alkaline pHs are optimized for MB photocatalytic degradation for studies.

In the process of photocatalytic degradation, the degradation efficiency depends on the amount of analyte dye adsorbed on the surface of the photocatalyst [50]. The effect of the initial concentration of MB on its photodegradation was carried out by varying the initial concentration from 5 to 20 ppm by keeping a fixed amount of Ru/Fe₃O₄ photocatalyst and the pH of the degradation solution. Figure 6 shows the degradation curves in both UV and sunlight irradiation with respect to different

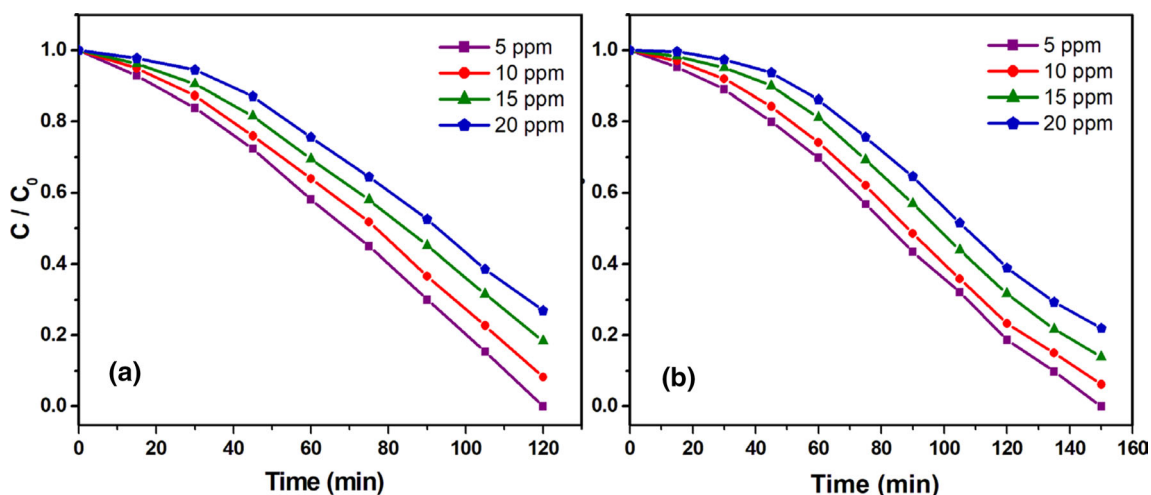


Fig. 6 Effect of initial concentration of MB under: a UV light and b sunlight using Ru/Fe₃O₄ photocatalysts

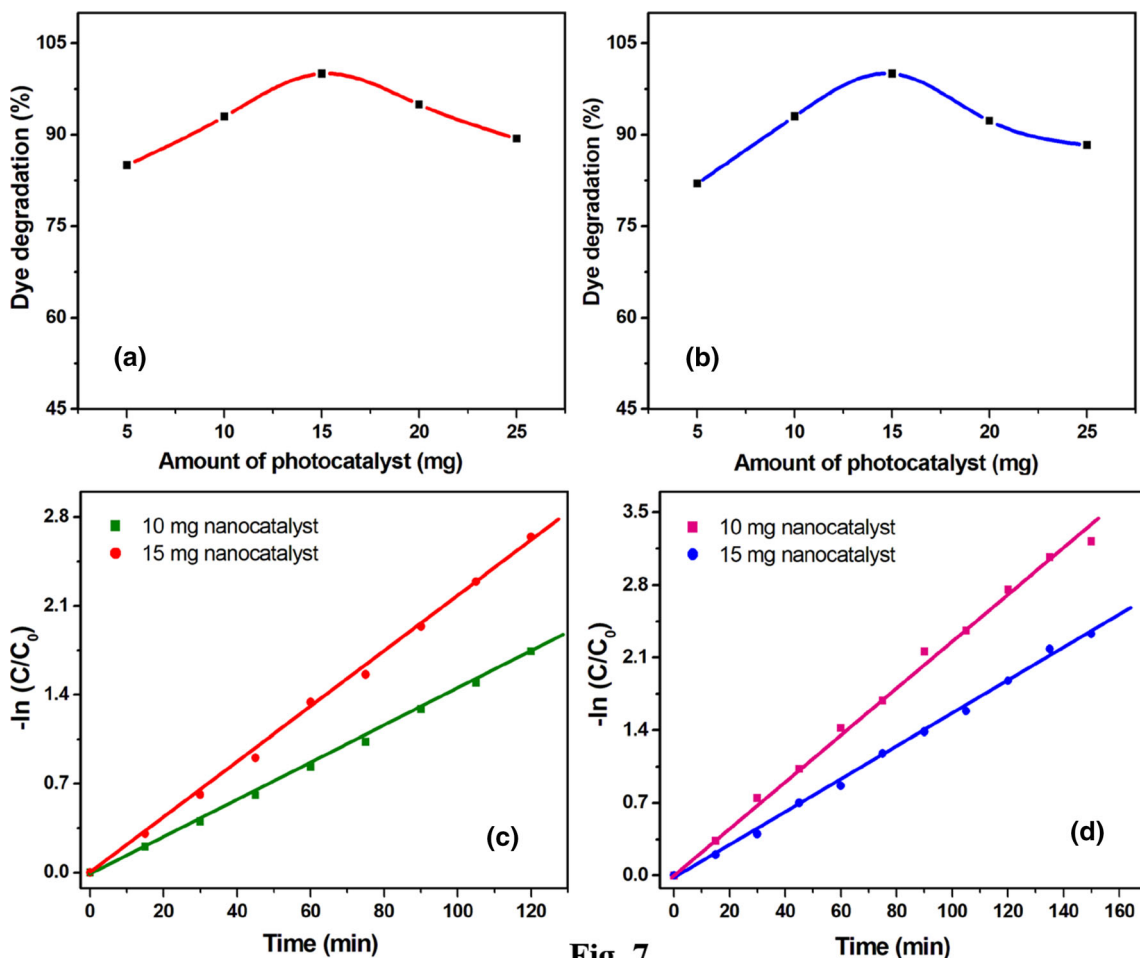


Fig. 7.

Fig. 7 Effect of Ru/Fe₃O₄ photocatalyst amount on photodegradation of MB under: a UV light and b sunlight; kinetic plots for the photocatalytic degradation of MB in c UV light and d in Sunlight

concentrations of MB. The results show that the photocatalytic degradation decreased with increasing MB concentration from 5 to 20 mg in both light exposures. A low

concentration of 5 mg achieves the highest photocatalytic degradation and at higher concentrations the degradation efficiency decreases. The increased concentration of MB

completely occupies the active sites, which leads to the saturation of the Ru/Fe₃O₄ photocatalyst surface and reduces the number of photons reaching the Ru/Fe₃O₄ surface [51]. This results in decrease of the generation of highly reactive hydroxyl radicals, which reduces the percentage of photocatalytic degradation.

The photocatalyst dosage is a significant parameter that can determine and achieve an effective photocatalytic degradation reaction. The effect of the Ru/Fe₃O₄ photocatalyst amount on the degradation of MB was investigated using different photocatalyst concentrations of 5, 10, 15, 20 and 25 mg/L, by maintaining constant experimental conditions of 5 mg/L of MB dye concentration and pH 11. Figure 7a & b illustrates the effect of photocatalyst dosage on the degradation efficiency. It has been observed that by increasing the amount of Ru/Fe₃O₄ photocatalyst, the photocatalytic degradation of MB increases. This is likely to be as the concentration of photocatalyst increases, the number of active sites on the surface of photocatalyst increases, leading to an increased generation of hydroxyl radicals and superoxide radicals [52]. These radicals are responsible for the actual photodegradation of the MB dye. The photocatalytic degradation increased to a certain dose of catalyst, then decreased slightly. This refers to the blockage of light radiation to the photocatalytic reaction due to the excess concentration of the photocatalyst. The other possible way is the excess amount of photocatalysts makes the photocatalysts to aggregate due to their high surface energy and surface area. As a result, the effective surface area of the photocatalyst decreases, resulting in a decrease in degradation performance.

Kinetics of MB Dye Degradation

Figure 7c, d presents the kinetic plots for the photocatalytic degradation of MB dye containing different amounts of Ru/Fe₃O₄ photocatalysts under UV light and sunlight radiation, respectively. Kinetic plots are constructed by plotting $-\ln(C/C_0)$ versus irradiation time (t, min) to estimate the photodegradation efficiency of MB using the following relation:

$$-\ln(C/C_0) = kt$$

where C₀ represents the initial concentration of MB dye (mg/L), C indicates the concentration of MB dye after

irradiation time 't', and 'k' is the degradation rate constant (min⁻¹). It can be seen from the kinetic plots (Fig. 7c & d) that a linear relationship between $-\ln(C/C_0)$ and irradiation time was found for the degradation of MB. Further, the photocatalytic degradation reaction of MB follows the pseudo first-order kinetics of the Langmuir–Hinshelwood model [53]. The degradation rate constants were estimated using the slopes of the regression lines and are listed in Table 1. The k value of 15 mg/L of the photocatalyst was shown to be higher than 10 mg/L. Also, the reaction rate constants under UV and sunlight irradiation are compared and show that the k value of UV light is larger than sunlight. This is due to the enhanced diffusion of MB molecules on the Ru/Fe₃O₄ surface, leading to faster electron–hole pair separation and increasing degradation efficiency accordingly [54]. The results suggest that an increase in the dosage of Ru/Fe₃O₄ nanocomposite photocatalyst from 10 to 15 mg/L increases the degradation rate of MB. Moreover, the additional loading of the photocatalyst may lead to a change in the photocatalytic degradation efficiency. This could be explained by the fact that the increased catalyst addition prevents light absorption and separation of charge carriers.

Identification of Reactive Oxidation Species

To explain the possible mechanism of photocatalytic degradation, it is necessary to identify the major reactive species involved in the photocatalytic process [55]. The photocatalytic oxidation process requires different reactive species such as holes (h⁺), hydroxyl (•OH) and superoxide radicals (•O₂⁻). For this study the photocatalytic experiments were performed under the same conditions in the presence of different scavengers. Ammonium oxalate (AO), isopropyl propanol (IPA) and benzoquinone (BQ) as scavengers of h⁺, •OH and •O₂⁻ species, respectively, were used to investigate the photocatalytic degradation of MB dye solution. Figure 8a displays the % MB dye degradation under UV/sunlight exposure before and after the addition of scavengers to the photocatalytic degradation solution. The results indicate that the addition of IPA significantly reduced the rate of degradation in both UV and sunlight irradiation, i.e. the photocatalytic degradation process progressed more effectively with •OH radicals. Using BQ, a lower rate of degradation was observed

Table 1 Kinetic parameters for photocatalytic degradation of MB dye

Light source	Amount of photocatalyst (mg/L ⁻¹)	k (min ⁻¹)	R ²
UV	10	0.0385	0.989
	15	0.0513	0.993
Sunlight	10	0.0294	0.981
	15	0.0402	0.990

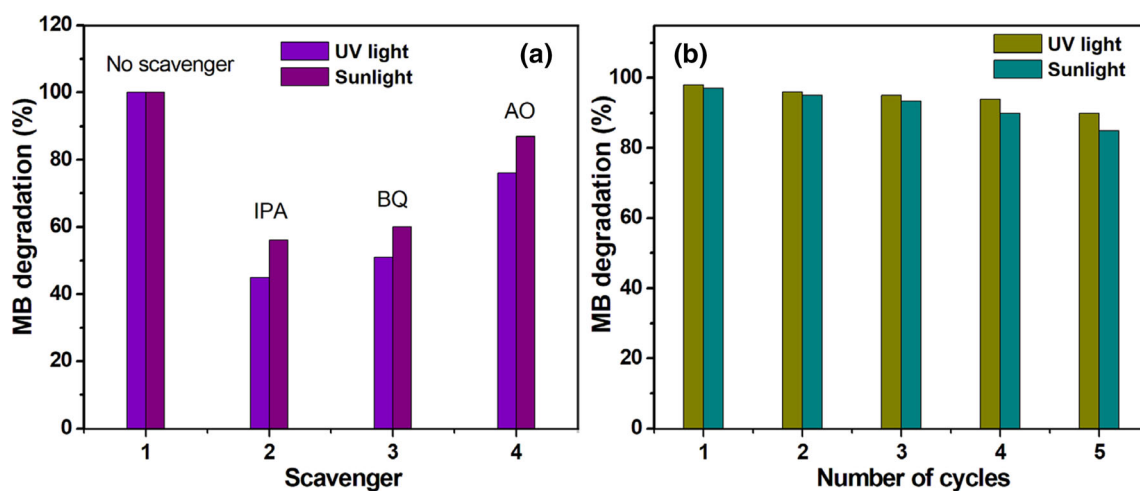


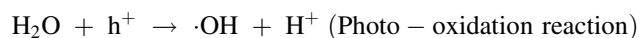
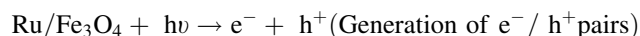
Fig. 8 **a** Effect of scavengers on photocatalytic degradation of MB (5 mg/L) and **b** photodegradation of MB using Ru/Fe₃O₄ photocatalysts on repeated cycles

compared to IPA, indicating that $\bullet\text{O}_2^-$ species also contribute to photocatalytic reactions. The addition of AO did not have a large effect on MB dye degradation. However, the performance of h^+ towards MB dye degradation cannot be completely eliminated. From these results two reactive species, $\bullet\text{OH}$ radicals and to some extent $\bullet\text{O}_2^-$ radicals play major role in the photocatalytic degradation of MB using Ru/Fe₃O₄ photocatalysts.

Mechanism of Photocatalytic Degradation

In the photodegradation reaction, the catalytic action of photocatalysts plays an important role. The reaction mechanism provides significant support for photocatalytic reactions that occur during the photodegradation process. The degradation efficiency of the photocatalytic process depends on the catalyst, nature of dye and the environment in which the reaction takes place. In this work, Fe₃O₄ is used as a base material to support Ru NPs, which differ in the energy levels between the valence band and the conduction band under UV/sunlight exposure. The difference in energy levels between Fe₃O₄ and Ru leads to the formation of electrons, which move from the surface of Ru to Fe₃O₄. The potential difference between the valence band holes (h^+) or the conduction band electrons (e^-) of Fe₃O₄ and Ru (two semiconductor materials) leads to electron migration. The transfer of photo-generated e^- from Ru (conduction band) to Fe₃O₄ (valance band) and h^+ from Ru (valance band) to Fe₃O₄ (valance band) may be thermodynamically favorable. The recombination of photo-generated e^- and h^+ is effectively decreased, which allows the nanocomposite to function longer and also enhances its photocatalytic ability [56].

Under the irradiation of UV/Sunlight, the electron–hole (e^-/h^+) pairs generated on the nanocomposite photocatalyst surface react with H₂O to obtain hydroxyl ($\bullet\text{OH}$) and superoxide radicals ($\bullet\text{O}_2^-$), which are required for the degradation of dye pollutants [57]. The relevant reaction formulas are given as follows:



The generation of hydroxyl and superoxide radicals is essential for the degradation dye pollutants during photocatalytic process. These highly reactive radicals formation occurs only under UV/Sunlight irradiation. In addition, the properties of the intermediate and decomposition compounds, including the size and charge of the material, have a significant impact on the degradation efficiency. The charge of the compounds in the degradation solution affects the adsorption on the surface of the photocatalyst. The availability of pores on the photocatalyst surface in various sizes is favorable for the adsorption of MB intermediates of different sizes.

Recycling of the Ru/Fe₃O₄ Photocatalysts

Recycling of photocatalysts plays a major role in practical applications [58]. The Ru/Fe₃O₄ photocatalysts were separated from the photodegradation reaction solution by applying an external magnetic field. The isolated photocatalysts were washed with deionized water and dried in an

oven set at 90 °C after every cycle of use. The recovered photocatalysts were again used for photodegradation of MB dye under similar experimental parameters. To examine the recyclability of Ru/Fe₃O₄ photocatalysts, the degradation efficiency was monitored for five cycles and the results are shown in Fig. 8b. The Ru/Fe₃O₄ photocatalyst exhibits reproducible results and the degradation efficiencies of MB up to four cycles are 94%. There after a decrease in the photocatalytic degradation efficiency was observed. The reduction of photodegradation might be because of the loss of few Ru/Fe₃O₄ nanocomposite particles into the solution and also adsorbed MB intermediates in the pore channels or on the photocatalyst's surface to reduce the absorption of light [59].

Conclusion

In summary, magnetic Ru/Fe₃O₄ photocatalysts were successfully synthesized in a single step by simple chemical co-precipitation method. The synthesized magnetic photocatalyst was characterized by different techniques and confirmed the formation of Ru NPs on Fe₃O₄ by TEM, TEM–EDX and XPS. The photocatalytic activity of synthesized nanocomposites was tested for degradation of MB dye in aqueous solution under UV and sunlight light radiation by varying several working parameters. It was found that a complete degradation of MB occurred in 120 and 150 min irradiation of UV and sunlight, respectively, and better photodegradation was observed under UV light. The photocatalytic degradation is likely to be greater in alkaline medium than in neutral and acid media. Furthermore, the degradation efficiency was increased by increasing the irradiation time and photocatalyst dosage, and decreased by increasing the initial MB concentration. An appropriate mechanism for the photocatalytic degradation of MB was given, in which the photodegradation process requires the formation of highly reactive hydroxyl and superoxide radicals. The developed Ru/Fe₃O₄ magnetic photocatalysts were easily separated from the solution using an external magnetic field and reused for up to five successive cycles without significant loss of photocatalytic activity. So, the synthesized magnetic Ru/Fe₃O₄ nanocomposite is an efficient photocatalyst for the degradation of MB under UV and sunlight irradiation.

Declarations

Conflict of interest The authors declare no conflict of interest.

References

1. S. Mahalingam, J. Ramasamy, and Y. H. Ahn (2018). *J. Clust. Sci.* **29**, 235. <https://doi.org/10.1007/s10876-017-1329-3>.
2. U. O. Bhagwat, K. R. Kumar, A. Syed, N. Marraiki, V. K. Ponnusamy, and S. Anandan (2021). *J. Clust. Sci.* <https://doi.org/10.1007/s10876-021-02053-0>.
3. M. Rani, U. Shanker, and V. Jassal (2017). *J. Environ. Manage.* **190**, 208. <https://doi.org/10.1016/j.jenvman.2016.12.068>.
4. S. A. Moghadam and F. Farzaneh (2021). *J. Clust. Sci.* <https://doi.org/10.1007/s10876-021-01994-w>.
5. D. Titus and E. J. J. Samuel (2019). *J. Clust. Sci.* **30**, 1335. <https://doi.org/10.1007/s10876-019-01585-w>.
6. S. Sarmah and A. Kumar (2011). *Indian J. Phys.* **85**, 713. <https://doi.org/10.1007/s12648-011-0071-1>.
7. K. Ravikumar, B. Deebika, and K. Balu (2005). *J. Hazard. Mater.* **122**, 75. <https://doi.org/10.1016/j.jhazmat.2005.03.008>.
8. J. Burhenne, K. D. Riedel, J. Rengelshausen, P. Meissner, O. Müller, G. Mikus, W. E. Haefeli, and I. Walter-Sack (2008). *J. Chromatogr. B Anal. Technol. Biomed. Life Sci.* **863**, 273. <https://doi.org/10.1016/j.jchromb.2008.01.028>.
9. M. R. Gaddekar and M. M. Ahammed (2020). *Appl. Water Sci.* **10**, 160. <https://doi.org/10.1007/s13201-020-01245-9>.
10. S. M. Alardhi, T. M. Albayati, and J. M. Alrubaye (2020). *Chem. Eng. Process. - Process Intensif.* **157**. <https://doi.org/10.1016/j.cep.2020.108113>.
11. D. Bhatia, N. R. Sharma, J. Singh, and R. S. Kanwar (2017). *Crit. Rev. Environ. Sci. Technol.* **47**, 1836. <https://doi.org/10.1080/10643389.2017.1393263>.
12. S. Wong, N. A. Ghafar, N. Ngadi, F. A. Razmi, I. M. Inuwa, R. Mat, and N. A. S. Amin (2020). *Sci. Rep.* **10**, 2928. <https://doi.org/10.1038/s41598-020-60021-6>.
13. F. Keyvani, S. Rahpeima, and V. Javanbakht (2018). *Solid State Sci.* **83**, 31. <https://doi.org/10.1016/j.solidstatesciences.2018.06.007>.
14. M. H. Abdel-Aziz, M. Bassyouni, M. S. Zoromba, and A. A. Alshehri (2019). *Ind. Eng. Chem. Res.* **58**, 1004. <https://doi.org/10.1021/acs.iecr.8b05291>.
15. A. P. Kumar, D. Bilehal, A. Tadesse, and D. Kumar (2021). *RSC Adv.* **11**, 6396. <https://doi.org/10.1039/d0ra10290c>.
16. S. Rahpeima, V. Javanbakht, and J. Esmaili (2018). *J. Inorg. Organomet. Polym. Mater.* **28**, 195. <https://doi.org/10.1007/s10904-017-0688-4>.
17. C. A. Ferreira, S. C. Domenech, and P. C. Lacaze (2001). *J. Appl. Electrochem.* **31**, 49. <https://doi.org/10.1023/A:1004149421649>.
18. M. Saquib and M. Muneer (2003). *Dye Pigment.* **56**, 37. [https://doi.org/10.1016/S0143-7208\(02\)00101-8](https://doi.org/10.1016/S0143-7208(02)00101-8).
19. I. Corsi, M. Winther-Nielsen, R. Sethi, C. Punta, C. Della Torre, G. Libralato, G. Lofrano, L. Sabatini, M. Aiello, L. Fiordi, F. Cinuzzi, A. Caneschi, D. Pellegrini, and I. Buttino (2018). *Ecotoxicol. Environ. Saf.* **154**, 237. <https://doi.org/10.1016/j.ecoenv.2018.02.037>.
20. H. Anwer, A. Mahmood, J. Lee, K. H. Kim, J. W. Park, and A. C. K. Yip (2019). *Nano Res.* **12**, 955. <https://doi.org/10.1007/s12274-019-2287-0>.
21. A. Rafiq, M. Ikram, S. Ali, F. Niaz, M. Khan, Q. Khan, and M. Maqbool (2021). *J. Ind. Eng. Chem.* **97**, 111. <https://doi.org/10.1016/j.jiec.2021.02.017>.
22. Y. Wang, J. Tao, X. Wang, Z. Wang, M. Zhang, G. He, and Z. Sun (2017). *Ceram. Int.* **43**, 4866. <https://doi.org/10.1016/j.ceramint.2016.12.130>.
23. A. Ahmad, S. H. Mohd-Setapar, C. S. Chuong, A. Khatoun, W. A. Wani, R. Kumar, and M. Rafatullah (2015). *RSC Adv.* **5**, 30801. <https://doi.org/10.1039/c4ra16959j>.

24. A. M. El-Khawaga, A. A. Farrag, M. A. Elsayed, G. S. El-Sayyad, and A. I. El-Batal (2020). *J Clust Sci.* <https://doi.org/10.1007/s10876-020-01869-6>.
25. A. Thamilselvan, P. Manivel, V. Rajagopal, N. Nesakumar, and V. Suryanarayanan (2019). *Colloid. Surf. B: Biointerfaces* **180**, 1. <https://doi.org/10.1016/j.colsurfb.2019.04.034>.
26. R. B. Song, S. Zhou, D. Guo, P. Li, L. P. Jiang, J. R. Zhang, X. Wu, and J. J. Zhu (2020). *ACS Sustain. Chem. Eng.* **8**, 1311. <https://doi.org/10.1021/acssuschemeng.9b07059>.
27. S. Sawan, R. Maalouf, A. Errachid, and N. Jaffrezic-Renault (2020). *TrAC - Trends Anal. Chem.* **131**, 116014. <https://doi.org/10.1016/j.trac.2020.116014>.
28. A. P. Kumar, M. W. Baek, C. Sridhar, B. P. Kumar, and Y. I. Lee (2014). *Bull. Korean Chem. Soc.* **35**, 1144. <https://doi.org/10.5012/bkcs.2014.35.4.1144>.
29. J. Wang, Z. Wei, S. Mao, H. Li, and Y. Wang (2018). *Energy Environ. Sci.* **11**, 800. <https://doi.org/10.1039/c7ee03345a>.
30. T. Umegaki, Y. Enomoto, and Y. Kojima (2016). *Catal. Sci. Technol.* **6**, 409. <https://doi.org/10.1039/c5cy00994d>.
31. S. Mondal, R. Singuru, S. Chandra Shit, T. Hayashi, S. Irle, Y. Hijikata, J. Mondal, and A. Bhaumik (2018). *ACS Sustain Chem Eng.* **6**, 1610. <https://doi.org/10.1021/acssuschemeng.7b02772>.
32. O. Długosz, K. Szostak, M. Krupiński, and M. Banach (2021). *Int. J. Environ. Sci. Technol.* **18**, 561. <https://doi.org/10.1007/s13762-020-02852-4>.
33. S. Kumar, T. Surendar, B. Kumar, A. Baruah, and V. Shanker (2013). *J. Phys. Chem. C.* **117**, 26135. <https://doi.org/10.1021/jp409651g>.
34. A. Sahoo and S. Patra (2020). *RSC Adv.* **10**, 6043. <https://doi.org/10.1039/c9ra08631e>.
35. R. M. Kulkarni, R. S. Malladi, M. S. Hanagadakar, M. R. Doddamani, B. Santhakumari, and S. D. Kulkarni (2016). *J. Mater. Sci. Mater. Electron.* **27**, 13065. <https://doi.org/10.1007/s10854-016-5449-6>.
36. Á. de J. Ruíz-Baltazar, (2021). *Ultrason. Sonochem.* **73**, 105521. <https://doi.org/10.1016/j.ultsonch.2021.105521>.
37. A. P. Kumar, B. P. Kumar, A. B. V. K. Kumar, B. T. Huy, and Y. I. Lee (2013). *Appl. Surf. Sci.* **265**, 500. <https://doi.org/10.1016/j.apsusc.2012.11.035>.
38. S. Ayni, M. Sabet, and M. Salavati-Niasari (2016). *J. Clust. Sci.* **27**, 315. <https://doi.org/10.1007/s10876-015-0931-5>.
39. M. Abbas, M. Takahashi, and C. Kim (2013). *J. Nanoparticle Res.* **15**, 1354. <https://doi.org/10.1007/s11051-012-1354-y>.
40. U. S. R. M. Cornell, *The iron oxides: structure, properties, reactions, occurrence, and uses* (Wiley-VCH, Weinheim, 1996).
41. A. Baranauskas, D. Jasaitis, and A. Kareiva (2002). *Vib. Spectrosc.* **28**, 263. [https://doi.org/10.1016/S0924-2031\(01\)00157-6](https://doi.org/10.1016/S0924-2031(01)00157-6).
42. C. P. Lin, S. B. Wen, and J. W. Halloran (2002). *J Am Ceram Soc.* **85**, 1467. <https://doi.org/10.1111/j.1151-2916.2002.tb00298.x>.
43. J. M. Campos-Martin, G. Blanco-Brieva, and J. L. G. Fierro (2006). *Angew Chemie - Int Ed.* **45**, 6962. <https://doi.org/10.1002/anie.200503779>.
44. M. C. Biesinger, B. P. Payne, A. P. Grosvenor, L. W. M. Lau, A. R. Gerson, and R. S. C. Smart (2011). *Appl. Surf. Sci.* **257**, 2717. <https://doi.org/10.1016/j.apsusc.2010.10.051>.
45. A. P. Grosvenor, B. A. Kobe, M. C. Biesinger, and N. S. McIntyre (2004). *Surf. Interface Anal.* **36**, 1564. <https://doi.org/10.1002/sia.1984>.
46. D. Chandra, Y. Inoue, M. Sasase, M. Kitano, A. Bhaumik, K. Kamata, H. Hosono, and M. Hara (2018). *Chem. Sci.* **9**, 5949. <https://doi.org/10.1039/c8sc01197d>.
47. J. F. Moulder, W. F. Stickle, P. E. Sobol, K. D. Bomben, Handbook of X-ray photoelectron spectroscopy: a reference book of standard spectra for identification and interpretation of XPS data, PerkinElmer Corp., Waltham, MA, 1992. <https://www.cnyunam.mx/~wencel/XPS/MANXPS.pdf>.
48. J. B. Coulter and D. P. Birnie (2018). *Phys. Status Solidi (b)* **255**, 1. <https://doi.org/10.1002/pssb.201700393>.
49. F. Karimi, H. R. Rajabi, and L. Kavoshi (2019). *Ultrason. Sonochem.* **57**, 139. <https://doi.org/10.1016/j.ultsonch.2019.05.019>.
50. F. Tavakoli, A. Badiei, F. Yazdian, G. M. Ziarani, and J. Ghasemi (2017). *J. Clust. Sci.* **28**, 2979. <https://doi.org/10.1007/s10876-017-1250-9>.
51. K. Azad and P. Gajanan (2017). *Chem Sci J.* **8**, 3. <https://doi.org/10.4172/2150-3494.1000164>.
52. L. Anju Chanu, W. Joychandra Singh, K. Jugeshwar Singh, and K. Nomita Devi (2019). *Results Phys.* **12**, 1230. <https://doi.org/10.1016/j.rinp.2018.12.089>.
53. Y. Li, X. Li, J. Li, and J. Yin (2006). *Water Res.* **40**, 1119. <https://doi.org/10.1016/j.watres.2005.12.042>.
54. S. R. Thawarkar, B. Thombare, B. S. Munde, and N. D. Khupse (2018). *RSC Adv.* **8**, 38384. <https://doi.org/10.1039/c8ra07404f>.
55. S. Mishra, M. Priyadarshinee, A. K. Debnath, K. P. Muthe, B. C. Mallick, N. Das, and P. Parhi (2020). *J. Phys. Chem. Solids* **137**. <https://doi.org/10.1016/j.colsurfa.2020.125551>.
56. N. Li, J. Zhang, Y. Tian, J. Zhao, J. Zhang, and W. Zuo (2017). *Chem. Eng. J.* **308**, 377. <https://doi.org/10.1016/j.cej.2016.09.093>.
57. X. Li, F. Chen, C. Lian, S. Zheng, Q. Hu, S. Duo, W. Li, and C. Hu (2016). *J. Clust. Sci.* **27**, 1877. <https://doi.org/10.1007/s10876-016-1049-0>.
58. Z. M. Abou-Gamra and M. A. Ahmed (2016). *J Photochem Photobiol B Biol.* **160**, 134. <https://doi.org/10.1016/j.jphotobiol.2016.03.054>.
59. C. H. Nguyen, C. C. Fu, and R. S. Juang (2018). *J Clean Prod.* **202**, 413. <https://doi.org/10.1016/j.jclepro.2018.08.110>.

Publisher's Note Springer Nature remains neutral with regard to jurisdictional claims in published maps and institutional affiliations.